Design of Optimal 2-D Nongrid Sparse Arrays for Medical Ultrasound

Bakary Diarra*, *Student Member, IEEE*, Marc Robini, *Member, IEEE*, Piero Tortoli, *Senior Member, IEEE*, Christian Cachard, and Hervé Liebgott, *Member, IEEE*

***Abstract*—Three-dimensional imaging with 2-D matrix probes is one of the most exciting recent ultrasound innovations. Unfortunately, the number of elements of a 2-D matrix probe is often very high, and reducing this number deteriorates the beam properties. In this paper, we propose a new sparse-array design technique with irregular element positioning, which significantly reduces the number of active elements as well as the grating-lobe level. In particular, we introduce a new cost function for optimizing the weighting coefficients of the elements and a new annealing-based algorithm to compute the lowest cost solutions. Numerical simulations show substantial improvements over standard sparse arrays.**

***Index Terms*—2-D array, 3-D imaging, simulated annealing, sparse array, ultrasound imaging.**

I. Introduction

ULTRASONIC imaging of a three-dimensional (3-D) region requires sweeping an ultrasound beam across a volume. In most available systems, this is done mechanically by manually moving a conventional linear or convex array, or, more frequently, by using a probe driven by a step motor [1]. However, these techniques are sensitive to the operator's skill and characterized by poor time resolution. These drawbacks can be overcome by using 2-D matrix arrays, which can be electronically controlled to steer the beams in both the elevation and lateral directions. Unfortunately, the design of a 2-D array probe must respect the spatial sampling condition (i.e., the pitch has to be smaller than half the wavelength), which imposes small-sized elements. Controlling such arrays is thus technically challenging because connecting and driving several hundreds (up to thousands) of elements is difficult, not to say unrealistic.

Possible approaches to reduce the number of coaxes in probe cables to a reasonable value (e.g., 256) include subaperture processors and microbeamformers [2]. In these cases, part of the beamformation is moved into the probe handle, requiring the development of sophisticated and expensive integrated circuits, with rigorous specifications in terms of dimensions and power consumption/dissipation [3]–[5]. Alternative methods have been proposed to reduce the number of elements while maintaining acceptable performance; the most efficient one is the random sparse-array technique [6] (hereafter referred to as the standard sparse-array technique). Since larger reductions of the number of active elements produce more severe deteriorations of the beam pattern (i.e., the spatial response of the array), the sparse-array techniques are typically combined with optimization algorithms to activate the most suitable elements.

Our first contribution is to show that a significant reduction of the grating-lobe level can be achieved by randomly placing the array elements. We call this technique the "nongrid" technique, because it does not restrict the possible element positions to a rectangular grid.

Our second contribution concerns the optimization task involved in sparse-array design, which is here based on the simulated annealing (SA) method [7], [8]. The best configurations are defined as the global minima of a cost function involving two terms: one measures how well the beam pattern matches a given template and the other one promotes sparsity by encouraging configurations with the smallest possible number of elements. In this paper, we propose a new cost function defined on a simple configuration space and whose sparsity-promoting term is convex, which substantially reduces the difficulty of the optimization problem. We also design an efficient SA algorithm that inherits the global convergence properties of finite-time annealing.

The paper is organized as follows. Section II reviews the state-of-the-art techniques in 3-D imaging and 2-D array element reduction. Section III gives a general description of the SA algorithm, and Section IV presents the nongrid technique along with the associated optimization scheme. In Section V, we compare our nongrid approach to the standard sparse-array technique in terms of beam characteristics and imaging capabilities. Discussion and conclusions are reported in Section VI.

Manuscript received December 18, 2012; revised April 15, 2013 and May 30, 2013; accepted June 1, 2013. Date of publication June 11, 2013; date of current version October 16, 2013. This work was supported in part by the Centre Lyonnais d'Acoustique (CeLyA) under ANR Grant 2011-LABX-014 and by the Italian Ministry of Education, Universities and Research under Grant PRIN 2010-2011. The work of B. Diarra was supported by the Franco-Italian University (VINCI Grant) and by the Rhone-Alpes region (Explora'Doc Grant). *Asterisk indicates corresponding author.*

*B. Diarra is with the Department of Electronics and Telecommunications, Università degli Studi di Firenze, Florence, Italy, and also with CREATIS, Université de Lyon, CNRS UMR 5220, INSERM U1044, Université Lyon 1, INSA-Lyon, Villeurbanne, Rhone 69100, France (e-mail: bakary.diarra@creatis.univ-lyon1.fr).

M. Robini, C. Cachard, and H. Liebgott are with the CREATIS, Université de Lyon, CNRS UMR 5220, INSERM U1044, Université Lyon 1, INSA-Lyon, Villeurbanne, Rhone 69100, France (e-mail: marc.robini@creatis.insa-lyon.fr; christian.cachard@creatis.insa-lyon.fr; liebgott@creatis.insa-lyon.fr).

P. Tortoli is with the Department of Electronics and Telecommunications, Università degli Studi di Firenze, Florence 50121, Italy (e-mail: piero.tortoli@unifi.it).

Color versions of one or more of the figures in this paper are available online at http://ieeexplore.ieee.org.

Digital Object Identifier 10.1109/TBME.2013.2267742

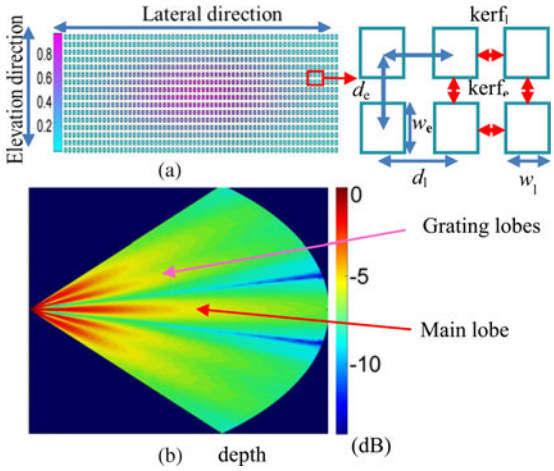

Fig. 1. 2-D array probe: (a) apodization coefficients (color bar) and spatial parameters; (b) associated beam pattern simulated by Field II in the lateral plane (the color bar represents the beam power).

II. State of the Art

A. 3-D Ultrasound Imaging

B-mode imaging with 1-D array probes has inherent limitations due to the 3-D nature of the structures to be observed. This makes it difficult to image the same plane at different times in follow-up studies, and physicians have to store several 2-D planes to reconstruct the entire structure under observation [1]. Three-dimensional ultrasound imaging has been developed to overcome these problems. It was initially based on manually moving a 1-D probe, which is quite sensitive to the operator's skill. Later, motorized displacement of 1-D probes permitted faster and more accurate acquisitions: this technique is used in obstetrics, cardiology, abdominal imaging [1], and surgical tool tracking [9]. However, mechanical 3-D imaging has limitations as well: it is time-consuming (the time needed to image a volume is on the order of 1 s) and it has poor resolution in the elevation direction.

In contrast, 2-D array probes have the capability of focusing ultrasonic beams in both the elevation and lateral directions and producing volumetric images in real time (about 20 volumes per second). Manufacturing such probes is a technical challenge because of the very large number of elements (for instance, the 2-D version of a classic 1-D 128-element array would have $128 \times 128 = 16\,384$ elements). In particular, the number of necessary connecting wires is unrealistic, and multiplexing can be used only if real-time performance is not essential to the target application [10], [11].

B. 2-D Array Beam Characteristics

A 2-D array probe consists of a set of rectangular elements aligned on a rectangular grid, as shown in Fig. 1(a) [12]. The beam pattern of a whole 2-D array [see Fig. 1(b)] includes the main lobe and the grating lobes. The latter are linked to the spatial periodicity of the elements and to their size relative to the wavelength. Side lobes can appear depending on the weighting (or apodization) coefficients and on the spatial distribution of the connected elements.

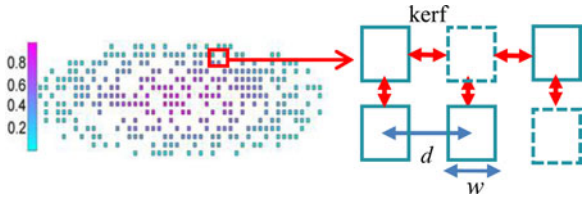

Fig. 2. Random sparse-array after edge-element deactivation (right, the dashed elements represent disconnected elements). The color bar represents the apodization.

To limit the grating-lobe level, the design of a 2-D array probe must respect the spatial sampling condition, that is, the interelement distance (pitch) must be smaller than half the wavelength, λ:

$$d_x = \mathrm{kerf}_x + \mathrm{w}_x < \lambda/2 \tag{1}$$

where d_x, w_x, and kerf_x denote the pitch, the element size, and the space between consecutive elements in the lateral direction ($x = 1$) or in the elevation direction ($x = e$).

C. Element Reduction Techniques

Because of the great technical difficulty in making dense-array probes (in which the elements are aligned on a rectangular grid and all connected), various techniques have been proposed to reduce the number of active elements. Row-column addressing is promising in terms of acquisition speed, but has a low SNR ratio and poor image resolution [10], [13]–[15]. The most widely used are edge-element deactivation and sparse-array techniques. Edge-element deactivation [16] simply consists in deactivating the "corner" elements so as to keep only the central ellipsoidal part of the matrix (or its central circular part if the matrix is square) [16]. This technique reduces the number of elements by approximately 20–30% [6], [10], [16], [17]. Since such a reduction usually is not sufficient, the technique must be combined with sparsification.

Sparse-array techniques periodically or randomly deactivate some elements of the 2-D array. The random sparse-array approach (illustrated in Fig. 2) is more promising because it does not increase the grating-lobe level compared to dense arrays. However, with this approach, the local interelement distance can be several times the original pitch, with consequences such as increased side-lobe level and energy loss [18].

A crucial aspect of random sparse-array techniques is to find the optimal set of active elements. The usual approach is to constrain the side-lobe level while keeping the width of the main lobe constant [7]; the solution is defined as any global minimum of a specific cost function (see, e.g., [7] and [4]) and is estimated by SA or by a genetic algorithm. Genetic algorithms are efficient for optimizing small 2-D arrays [8], but SA shows better performance for large arrays in terms of speed and robustness. Since our interest here is the design of large 2-D arrays, we focus on SA, which is discussed in the following section.

III. Simulated Annealing

The application of SA to sparse-array design was first suggested by Trucco [7] and recently refined by Chen *et al.* [8].

The key feature of SA is that it allows uphill moves (that is, moves that increase the value of the objective function) in order to escape local minima. By analogy with the physical process of annealing in solids, uphill moves are accepted with a certain probability controlled by a temperature parameter that decreases monotonically to zero. Section III-A below gives a formal description of SA, followed by the main convergence results in Section III-B.

A. Simulated Annealing Algorithm

Let f be a real-valued function to be minimized on a general but finite state space E. An SA algorithm with cost function f is a discrete time, nonhomogeneous Markov chain $\left(\Gamma^{(n)}\right)_{n\geq 0}$ whose transitions are guided by a communication mechanism q and controlled by a cooling sequence $(T_n)_{n\geq 1}$. The communication mechanism gives the probabilities of the possible moves for generating a candidate solution from the current solution, and the cooling sequence decreases to zero. Formally, q is a map from E^2 to [0,1] that has the following properties.

1) q is a Markov matrix: $\sum_{\eta\in E} q(\gamma,\eta)=1$ for all $\gamma\in E$.
2) q is symmetric: $q(\gamma,\eta)=q(\eta,\gamma)$ for all $(\gamma,\eta)\in E^2$.
3) q is irreducible: for any $(\gamma,\eta)\in E^2$, there is a path $\gamma^{(1)},\ldots,\gamma^{(K)}$ such that $\gamma^{(1)}=\gamma,\gamma^{(K)}=\eta$, and $q\left(\gamma^{(k)},\gamma^{(k+1)}\right)>0$ for all $k\in\{1,\ldots,K-1\}$.

(Property 2 means that the probability of proposing a move from γ to η is the same as the probability of proposing a move from η to γ, and property 3 means that any state can be reached from any other state in a finite number of moves.) The transitions of $(\Gamma^{(n)})_n$ are given by

$$\mathrm{P}(\Gamma^{(n)}=\eta|\Gamma^{(n-1)}=\gamma)=P_{T_n}(\gamma,\eta) \tag{2}$$

where P_T is the Markov matrix on E defined by

$$P_T(\gamma,\eta)=\begin{cases} q(\gamma,\eta) \text{ if } f(\eta)\leq f(\gamma) \text{ and } \eta\neq\gamma \\ q(\gamma,\eta)\exp(-(f(\eta)-f(\gamma))/T) \text{ if } f(\eta)>f(\gamma). \end{cases} \tag{3}$$

Putting it simply, downhill moves are unconditionally accepted, whereas an uphill move from γ to η at iteration n is accepted with the probability $\exp(-(f(\eta)-f(\gamma))/T_n)$. In practice, a finite-time realization $\left(\gamma^{(n)}\right)_{0\leq n\leq N}$ of $\left(\Gamma^{(n)}\right)_n$ is generated as follows:

pick an initial state $\gamma^{(0)}\in E$;
for $n=1$ to N **do**
  draw a state η from the probability distribution $q(\gamma^{(n-1)},\,.\,)$ on E;
  set $\gamma^{(n)}\leftarrow\gamma^{(n-1)}$;
  set $\Delta\leftarrow f(\eta)-f(\gamma^{(n-1)})$;
  if $\Delta\leq 0$ **then** set $\gamma^{(n)}\leftarrow\eta$;
  else set $\gamma^{(n)}\leftarrow\eta$ with probability $\exp(-\Delta/T_n)$;
  end (if)
end (for)

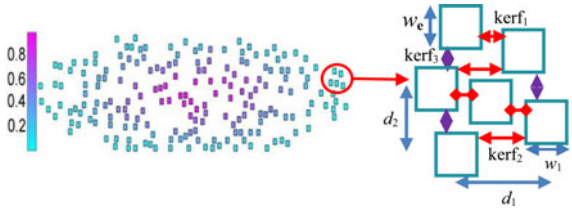

Fig. 3. Nongrid-based random sparse array.

B. Main Convergence Results

As the temperature T_n goes to zero, the distribution of $\Gamma^{(n)}$ concentrates on the global minima of f, and SA does indeed converge to a global minimum if $T_n\propto 1/\ln(n+1)$ [19]. However, logarithmic cooling yields extremely slow convergence, and most successful SA applications use exponential schedules. The theoretical justification of exponential cooling is given in [20], where it is shown that the convergence speed exponent of SA has an upper limit α_{opt} and that it is possible to construct a family $\left\{(T_n)_{1\leq n\leq N}\,;N\geq 1\right\}$ of finite cooling sequences as

$$T_n=T_0\exp(-\zeta n) \tag{4}$$

where $\zeta\in(0,+\infty)$ depends on N, such that

$$\ln\left(\mathrm{P}\left(f(\Gamma^{(N)})>\inf_{\gamma\in E} f(\gamma)\right)\right)\sim\ln\left(N^{-\alpha_{\mathrm{opt}}}\right). \tag{5}$$

These results are not well known, and yet they constitute the most significant advance in SA theory beyond the asymptotic properties established in [19]. They imply in particular that for any $\alpha\in(0,\alpha_{\mathrm{opt}})$ there is a family $\left\{(T_n)_{1\leq n\leq N}\,;N\geq 1\right\}$ of finite exponential cooling sequences such that

$$\mathrm{P}\left(f(\Gamma^{(N)})>\inf_{\gamma\in E} f(\gamma)\right)\sim N^{-\alpha} \tag{6}$$

for a large enough N. In other words, exponential cooling makes it possible for SA to have a convergence speed exponent arbitrarily close to the best achievable exponent over all possible cooling sequences. More elaborate developments in SA theory can be found in [21] and [22].

IV. Contributions

A. Random Element Positioning

In standard random sparse arrays (see Fig. 2), the centers of the active elements are placed on the points of a rectangular grid with spacing equal to $\lambda/2$ [7], [8]. However, the probe performance is limited by this positioning constraint and can be significantly improved by randomly setting the element positions. More precisely, we propose a nongrid approach in which the elements can be placed anywhere on the surface of the probe provided they do not overlap. An example of a probe based on such irregular placement is given in Fig. 3; the kerf and the pitch between neighboring elements are no longer constant and can be viewed as the realizations of random variables. The set of possible element positions is obtained by randomly sampling the surface of the probe and by discarding each new sample that introduces overlapping.

B. Cost Function

A general cost function including the parameters of our optimization problem—namely, the set of active elements and the maximum side-lobe level—was proposed by Trucco [7] (see also [23]) and refined in [8]. We start with a modified description of this function, which will serve as a basis for discussing our choice.

Assume that each possible element position is indexed by an integer $m \in \{1, \ldots, M\}$, where M is the total number of positions. Then any sparse-array configuration can be represented by a set $A \subset \{1, \ldots, M\}$ defining the active elements and by a vector $\gamma \in [\gamma_{\min}, \gamma_{\max}]^{|A|}$ containing the weighting coefficients of these elements. More precisely, for any $i \in \{1, \ldots, |A|\}$, the ith entry γ_i of γ is the weighting coefficient of the active element $\sigma_A(i)$, where σ_A is the bijection from $\{1, \ldots, |A|\}$ to A such that $\sigma_A(1) < \cdots < \sigma_A(|A|)$. Using this representation, the set S of all possible sparse-array configurations is given by

$$S = \{(A, \gamma) : A \subset \{1, \ldots, M\} \text{ and } \gamma \in [\gamma_{\min}, \gamma_{\max}]^{|A|}\}. \tag{7}$$

Let $p(A, \gamma)$ be the normalized far-field beam pattern [24] of the array (A, γ), that is,

$$p_{(A,\gamma)}(u, v) = \frac{1}{\|\gamma\|_1} \left| \sum_{i=1}^{|A|} \gamma_i \exp\left(\frac{2j\pi}{\lambda} \left(x_{\sigma_A(i)} u + y_{\sigma_A(i)} v \right) \right) \right| \tag{8}$$

where $u, v \in [-2, 2]$ are the first two coordinates of the difference between the unit arrival and steering directions, $\|\gamma\|_1 = \sum_{i=1}^{|A|} |\gamma_i|$ is the l_1-norm of γ, and (x_m, y_m) denotes the position of the mth element on the surface of the probe. The optimization problem considered in [7] is equivalent to that of minimizing the function $f_{\mathrm{T}} : S \to \mathbb{R}$ defined by

$$f_{\mathrm{T}}(A, \gamma) = \mu |A| + \iint_U \left(p_{(A,\gamma)}(u, v) - p_{\mathrm{s}} \right)^+ \mathrm{d}u \, \mathrm{d}v \tag{9}$$

where $\mu > 0$ controls the strength of the sparsity constraint, p_s is the maximum side-lobe authorized outside the main-lobe region, t^+ stands for the positive part of t (that is, $t^+ = \max(\{t, 0\})$), and U is the set of coordinate pairs (u, v) outside the main-lobe region.

To define our cost function, we first simplify the manipulation of the array configurations by representing them by vectors in a subset E of the closed rectangle $[0, \gamma_{\max}]^M$. Then, the mth element of an array γ is active if $\gamma_m > 0$, and the sparsity promoting functional used in (9) is the l_0-norm $\|.\|_0 : \gamma \in E \to |\{m : \gamma_m \neq 0\}|$. We propose to further reduce the complexity of the optimization problem by replacing the l_0-norm with the l_1-norm $\|.\|_1 : \gamma \in E \to \sum_{m=1}^{M} |\gamma_m|$, which, unlike the l_0-norm, is continuous and convex (the use of the l_1-norm as a sparsity-promoting functional is reviewed in [25] and [26]). The solutions to this optimization problem are thus the global minima of the cost function $f : E \to \mathbb{R}$ defined by

$$f(\gamma) = \mu \|\gamma\|_1 + \left(\iint_U \left(p_{(A,\gamma)}(u, v) - p_{\mathrm{s}} \right)^+ \mathrm{d}u \, \mathrm{d}v \right)^2 \tag{10}$$

(taking the square of the integral rather than the integral itself is merely a matter of choice), where the beam pattern p_γ is given by

$$p_\gamma(u, v) = \frac{1}{\|\gamma\|_1} \left| \sum_{m=1}^{M} \gamma_m \exp\left(\frac{2j\pi}{\lambda} \left(x_m u + y_m v \right) \right) \right|. \tag{11}$$

Minimizing f over E is significantly easier than minimizing f_{T} over S, but it remains a difficult optimization problem nonetheless, which is why we also use SA. It is important to realize that the computed solutions are not sparse in the strict sense, in that their entries are mostly zeros; they are sparse in the weak sense, in that a great proportion of their entries are very close to zero. Consequently, the final solution is obtained by applying a hard threshold to the entries of the output of the minimization process. Denoting this output by $\hat{\gamma}$, the weighting coefficients $\gamma_1^*, \ldots, \gamma_M^*$ of the optimized sparse array are given by

$$\gamma_m^* = \begin{cases} \hat{\gamma}_m & \text{if } \hat{\gamma}_m \geq \tau \\ 0 & \text{if } \hat{\gamma}_m < \tau \end{cases} \tag{12}$$

where τ is a predefined threshold.

C. Optimization by Simulated Annealing

Designing an efficient SA algorithm means intelligently choosing the communication mechanism q and carefully selecting the cooling sequence $(T_n)_{n \geq 1}$. In this section, we describe our communication strategy and the associated SA algorithm. The tuning of the cooling sequence is discussed in Section IV-D.

First of all, to satisfy the finite-state space assumption of the SA theory outlined in Section III-B, we let the domain of f be the discrete set

$$E = \Lambda^M, \quad \Lambda = \left\{ \frac{l \gamma_{\max}}{L} : l \in \{0, \ldots, L\} \right\} \tag{13}$$

where the positive integer L can be arbitrarily large. That said, we use a communication mechanism that generates candidate solutions that differ from the current states by at most one element, as in [7] and [8]. However, since the representation of the sparse-array configurations as elements of E (13) is simpler than the representation in S (7), our single-element updating dynamics is simpler than those proposed in [7] and [8]. Indeed, we generate a candidate solution $\eta = (\eta_1, \ldots, \eta_M)$ from a configuration $\gamma = (\gamma_1, \ldots, \gamma_M)$ by selecting an element index $k \in \{1, \ldots, M\}$ and a weighting coefficient $c \in \Lambda$ uniformly at random and setting $\eta_k = c$ and $\eta_m = \gamma_m$ for all $m \neq k$. Formally, the associated communication matrix has a quite simple expression: for any $(\gamma, \eta) \in E^2$,

$$q(\gamma, \eta) = \begin{cases} 1/(M(L+1)) & \text{if } \exists! k \in \{1, \ldots, M\}, \eta_k \neq \gamma_k \\ 1/(L+1) & \text{if } \eta = \gamma \\ 0 & \text{otherwise.} \end{cases} \tag{14}$$

This Markov chain is clearly symmetric and irreducible, which are the two requirements on the communication mechanism for the convergence of SA.

The exponential cooling sequence (4) can be written as

$$T_n = T_{\max}\left(\frac{T_{\min}}{T_{\max}}\right)^{\frac{n-1}{N-1}} \tag{15}$$

where $T_{\max}$ and $T_{\min}$ denote the initial and final temperatures, respectively, and N is the total number of iterations. Given these parameters, and letting ε^k be the kth vector of the standard basis of $\mathbb{R}^M$, the pseudocode of our SA algorithm for sparse-array optimization is the following:

set $\xi \leftarrow \ln(T_{\min}/T_{\max})/(N-1)$;
for $n = 1$ **to** N **do**
  draw $k \in \{1, \ldots, M\}$ and $c \in \Lambda$ uniformly at random;
  set $\eta \leftarrow \gamma^{(n-1)} + (c - \gamma_k^{(n-1)})\varepsilon^k$;
  set $\Delta \leftarrow f(\eta) - f(\gamma^{(n-1)})$;
  if $\Delta \leq 0$ **then** set $\gamma^{(n)} \leftarrow \eta$;
  else
    set $T \leftarrow T_{\max}\exp((n-1)\xi)$;
    draw $a \in [0,1]$ uniformly at random;
    if $a \leq \exp(-\Delta/T)$ **then** set $\gamma^{(n)} \leftarrow \eta$;
    else set $\gamma^{(n)} \leftarrow \gamma^{(n-1)}$;
    end (if)
  end (if)
end (for)

D. Tuning of the Cooling Sequence

The performance of an SA algorithm is strongly influenced by the tuning of its cooling sequence. Making a dichotomy between the asymptotic and finite-time convergence theories, one can use either logarithmic or exponential cooling. For instance, Trucco [7] uses logarithmic sequences

$$T_n = \frac{T_{\max}\ln(2)}{\ln(\kappa M\lfloor n/M\rfloor + 2)} \tag{16}$$

where $\kappa > 1$, and $\lfloor . \rfloor$ is the floor function, whereas Chen *et al.* [8] use exponential sequences

$$T_n = T_{\max}\tau^{\lfloor n/M\rfloor} \tag{17}$$

with $\tau = 0.85$. In both cases, the temperature is updated after each sweep (that is, after each cycle through all the elements), and the initial temperature $T_{\max}$ is chosen empirically so that most transitions are accepted at the beginning of the annealing process. The final temperature can be fixed in advance by setting the number of sweeps, as in [7], or it can be set adaptively via a termination criterion, as in [8], where it is proposed to stop the algorithm when the number of active elements does not decrease over a given number of sweeps.

Contrary to [7], we suggest using exponential cooling, which is more robust than logarithmic cooling in the finite-time case [20], and unlike [8], we prefer to fix the horizon N of the algorithm so as to keep control over the runtime. This leaves us with the problem of finding appropriate values for the initial and final temperatures, which was extensively addressed in the early stages of SA development (see, e.g., [27]). From our experience, we suggest selecting $T_{\max}$ and $T_{\min}$ so that the uphill acceptance rates (that is, the ratios of the number of accepted uphill moves to the number of proposed uphill moves) at the beginning and at the end of the optimization process are close to the given values $\chi_{\max}$ and $\chi_{\min}$ such as $0 < \chi_{\min} \ll \chi_{\max} < 1$. Accurate methods to perform these estimations are given in [28], but they are time consuming. In fact, as long as the horizon N is large enough, correct orders of magnitude are satisfactory, and thus fast appropriate estimation methods do the job.

We propose a simple and efficient procedure based on the homogeneous Markov chain $(\Gamma^{(n)})_n$ with the transition probabilities

$$\mathrm{P}\left(\Gamma^{(n)} = \eta | \Gamma^{(n-1)} = \gamma\right) = q(\gamma, \eta) \tag{18}$$

where q is the communication matrix defined in (14). Given a positive integer K, we generate a finite-time realization of $(\Gamma^{(n)})_n$ with K uphill moves, and we set $T_{\max}$ and $T_{\min}$ to be the temperature values such that the average acceptance probabilities over these uphill moves are equal to $\chi_{\max}$ and $\chi_{\min}$, respectively. More formally, we simulate $(\Gamma^{(n)})_n$ until we obtain K pairs $(\gamma^{(n_k)}, \gamma^{(n_k+1)})$ of successive states such that $f\left(\gamma^{(n_k)}\right) < f\left(\gamma^{(n_k+1)}\right)$, and we let $T_{\max}$ and $T_{\min}$ be the solutions of

$$\frac{1}{K}\sum_{k=1}^{K}\exp(-(f(\gamma^{(n_k+1)}) - f(\gamma^{(n_k)}))/T) = \chi \tag{19}$$

for $\chi = \chi_{\max}$ and $\chi = \chi_{\min}$. The left-hand side of (19) increases with increasing temperature, and thus, for any $\chi \in (0,1)$, this equation has a unique solution that can be determined by any standard root-finding method. In practice, effective cooling sequences are obtained by taking $\chi_{\max} \in [0.6, 0.9]$, $\chi_{\min} \in \left[10^{-4}, 10^{-3}\right]$, and K on the order of 10 to 100 times the number M of possible element positions.

V. Simulation Results

This section reports our simulations performed with Field II [29], [30] to assess the performance of the nongrid technique. All our results correspond to simulations of the two-way beams obtained by locating a scatterer in a fixed position and by steering the transmitted beam over a wide range of angles (typically from $-90°$ to $90°$). The transmit (TX) and receive (RX) foci are set to coincide with the scatterer depth.

Two reference dense arrays are considered: a square 64 × 64 grid and a rectangular 64 × 16 grid, both with deactivated edge elements [16]. The sizes of these dense array probes are 17 mm × 17 mm and 17 mm × 4.2 mm, respectively. (The latter dimensions were suggested by our physicians for possible liver biopsy applications requiring intercostal imaging.) The elements are squares. In the 4:1 rectangular case, the direction of the largest dimension of the probe is called the lateral direction, and the other is called the elevation direction. In the square case there is no distinction since the beam is symmetric.

The standard and the nongrid sparse arrays are derived from the dense arrays by using the methods described in Sections II-C and IV-A, respectively. The performance of sparse arrays with

TABLE I
SIMULATION PARAMETERS USED FOR STUDYING THE INFLUENCE OF THE NUMBER OF ACTIVE ELEMENTS

Central frequency	3.5 MHz
Wavelength (λ)	0.44 mm
Element size	0.22 mm × 0.22 mm
Pitch (d)	0.264 mm

and without grid-positioning constraints is systematically compared. Sections V-A and V-B describe the influence of the number of active elements and their size. Section V-C illustrates our method for sparse-array optimization, and in Section V-D a biopsy needle inserted in a homogeneous tissue and a cyst phantom, respectively, are imaged with multiple RX foci.

A. Influence of the Number of Active Elements

For standard sparse arrays, the condition (1) corresponds to widening the main lobe. Hence, a pitch value slightly above half the wavelength is a good tradeoff. We set $d = 0.6\lambda$ and $w = 0.5\lambda$, and we use the simulation parameters given in Table I (the pitch value is not significant for nongrid sparse arrays). A number of elements ranging between 64 and 1024 are activated in the square case and between 64 and 576 in the 4:1 rectangular case. The positions of the activated elements are randomly selected when there is no grid constraint.

The results are presented in box plots in which each box summarizes the statistics of 100 simulations for a fixed number of active elements (the upper and lower edges of each box represent the 75th and 25th percentiles, respectively, and the central mark is the median). The rationale for this type of representation is to provide a comparison between standard and nongrid arrays that is independent of the optimization method. Fig. 4 displays the statistics of the grating-lobe levels in the lateral and elevation directions as functions of the number of active elements. The grating-lobe level of nongrid arrays is significantly lower and decreases faster than that of standard arrays. For square probes, the average reduction of the grating-lobe level produced by random element-positioning ranges from -3 to -15 dB. In the 4:1 rectangular example, this reduction ranges from -3 to -17 dB in the lateral direction and from -12 to -27 dB in the elevation direction.

Moreover, as illustrated in Fig. 5, random-element positioning does not increase the width of the main lobe. More precisely, the statistics of the main-lobe width of nongrid sparse arrays are similar to that of standard sparse arrays, except for the elevation direction of the 4:1 rectangular probes in which case random-element placement produces thinner main lobes as the number of active elements increases above 128.

B. Influence of Element Size

The element size has an important effect on the beam characteristics, especially on probe sensitivity [31] and on the grating lobes. The larger the elements, the narrower the main lobe, but at the same time the grating lobes increase and get closer to the main lobe. Therefore, a tradeoff must be made between the main lobe and the grating lobes of the beam pattern.

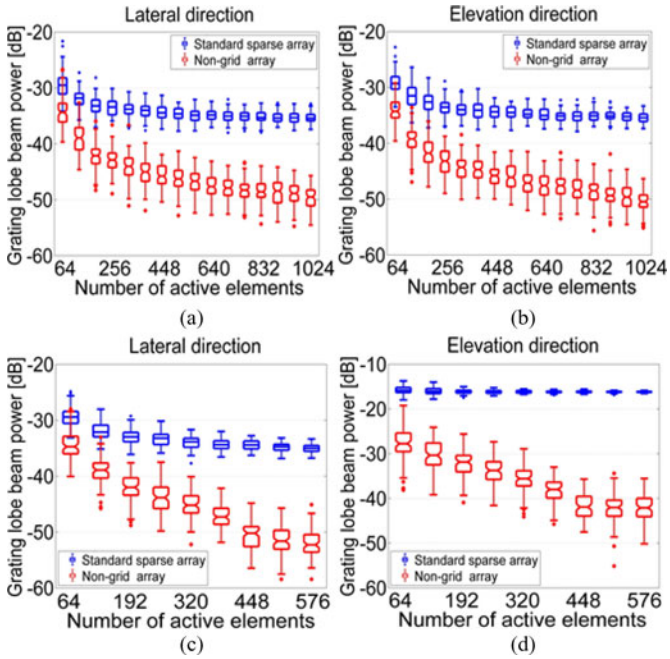

Fig. 4. Grating-lobe level in the lateral and elevation directions as a function of the number of active elements (each box represents 100 simulations): (a), (b) square probes; (c), (d) 4:1 rectangular probes.

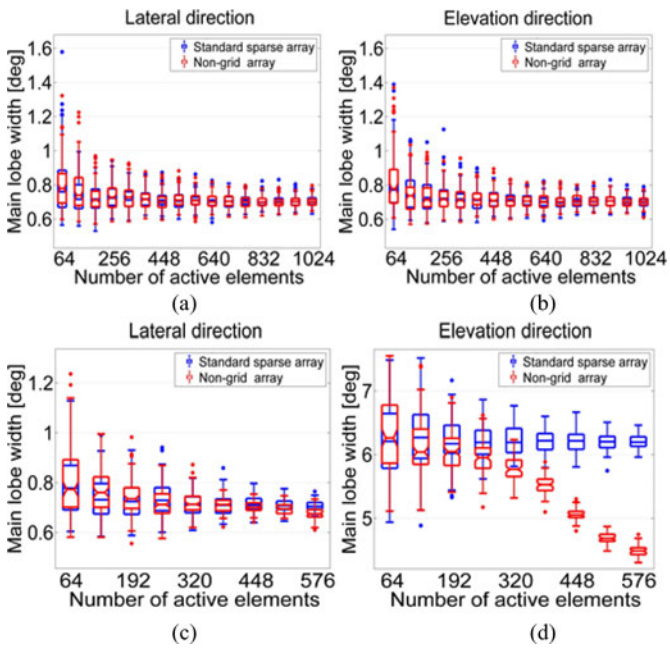

Fig. 5. Main-lobe width as a function of the number of active elements (each box represents 100 simulations): (a), (b) square probes; (c), (d) 4:1 rectangular probes.

Figs. 6 and 7 show the grating-lobe level and the width of the main lobe obtained with standard and nongrid sparse arrays when the element size varies between $\lambda/5$ and λ. The number of active elements has been set to 256 for the square case and to 100 for the rectangular case. Each box summarizes the statistics of 100 simulations for a fixed element size. The grating-lobe

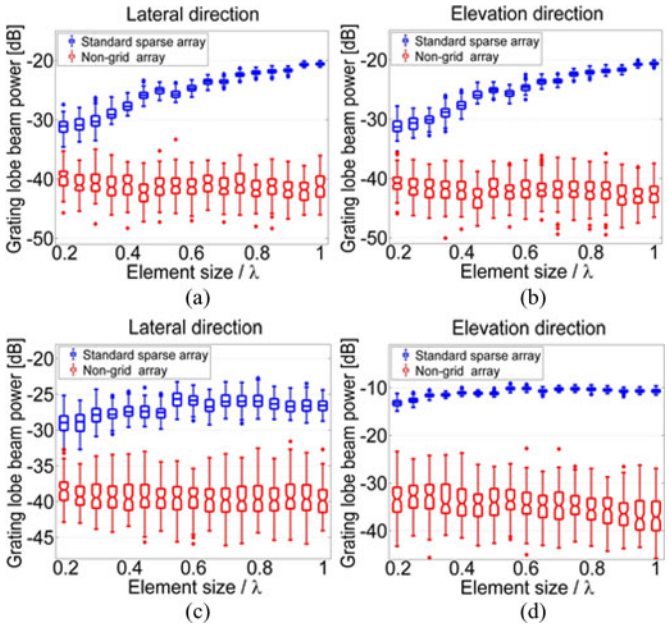

Fig. 6. Grating-lobe level as a function of the element size (each box represents 100 simulations): (a), (b) square probes with 256 active elements; (c), (d) 4:1 rectangular probes with 100 active elements.

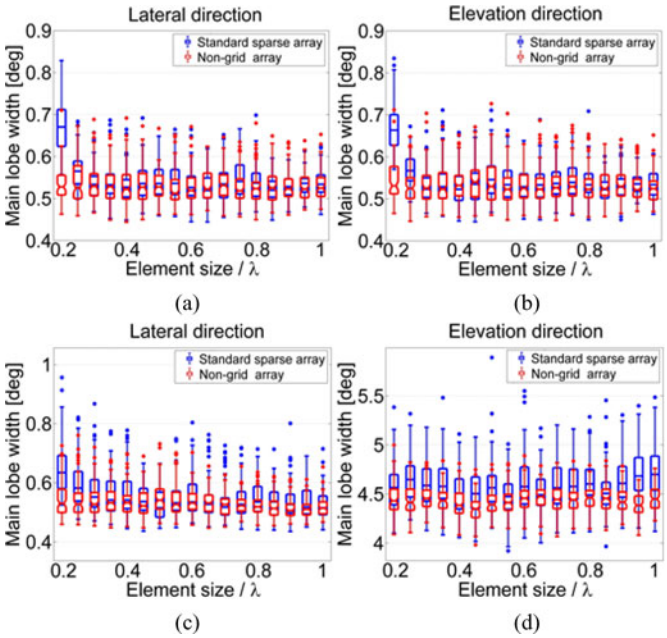

Fig. 7. Main-lobe width as a function of the elements' size (each box represents 100 simulations): (a), (b) square probes with 256 active elements; (c), (d) 4:1 rectangular probes with 100 active elements.

level of standard sparse arrays tends to increase with increasing element size, while the grating-lobe level of nongrid sparse arrays remains approximately constant. Moreover, the latter is 9–25 dB lower than the level obtained with standard sparse arrays. In addition, Fig. 7 shows that nongrid positioning does not increase the width of the main lobe but even slightly reduces it in the elevation direction.

C. Optimized Sparse Arrays

The SA-based standard and nongrid sparse array optimization described in Section IV has been tested on both the square and the rectangular probe. The number, *M,* of elements was set to 3348 and 728, coincident with the number of elements occupying the central circular and ellipsoidal part of the 64 × 64 and 64 × 16 dense arrays, respectively. The element size was λ/2 for the standard sparse array and 4λ/5 (any value between λ/2 and λ could be used) for the nongrid sparse array. Performance is measured in terms of main-lobe width and side-lobe and grating-lobe levels in the lateral and elevation directions. The goal is to obtain an array with less than 256 elements, so that its implementation is manageable.

As stated above, in standard sparse arrays the possible element positions are aligned on a Cartesian grid, whereas in the case of the nongrid sparse array, the set is randomly determined with the constraint that no elements overlap. Given the initial positions, our cost function f, defined in (10), is fully specified by: 1) the main-lobe region, which is defined as the interior of a circle (for square arrays) or of an ellipse (for rectangular arrays) with the principal axes parallel to the lateral and elevation directions, 2) the maximum side-lobe level p_{s}, and 3) the parameter μ, which controls the tradeoff between beam pattern constraints and sparsity. We set the main-lobe region to fit the -6 dB widths of the main lobe of the corresponding dense array. This width, for the square array, is 0.7° in both directions, while for the rectangular array is 0.7° and 6.2° in the lateral and the elevation direction, respectively. The maximum sidelobes level is $p_{\mathrm{s}} = -40$ dB [32]. The parameter μ was empirically chosen as the value that gives the best results, namely $\mu = 4.10^{-5}$.

The state space E (13) is defined by $\gamma_{\max} = 1.5$ and $L = 1.5 \times 10^4$, and the solutions are computed as follows: first, we compute an estimate $\hat{\gamma}$ of the global minimum of f using the SA algorithm described in Section IV-C, starting from an initial configuration $\gamma^{(0)}$ chosen uniformly at random; second, we apply a hard threshold of 0.2 to the entries of $\hat{\gamma}$ to obtain the optimized sparse array γ^* [see (12)]. Therefore, the set of active elements of the optimized sparse array is $\{m : \hat{\gamma}_m \geq 0.2\}$ and the weighting coefficients of these active elements are within $[0.2, 1.5]$. The length N of the annealing chain is set to 1024 *M,* and the cooling sequence is of the type reported in (15), where the initial and final temperatures $T_{\max}$ and $T_{\min}$ are selected using the method described in Section IV-D with $\chi_{\max} = 0.8$ and $\chi_{\min} = 10^{-3}$.

The optimized square sparse arrays are shown in Fig. 8, together with their beam profiles along the lateral directions. The standard sparse array [Fig. 8(a)] has 216 active elements, while the nongrid sparse array [Fig. 8(b)] has 186 elements. The two-way beam profiles shown in Fig. 8(c) were obtained by placing a scatterer at a 40-mm depth along the probe axis. The -6 dB lateral (and elevation) width of the main lobe is about 0.63° for both the standard and nongrid sparse arrays. We can see from Fig. 8(c) that both arrays satisfy the maximum side-lobe

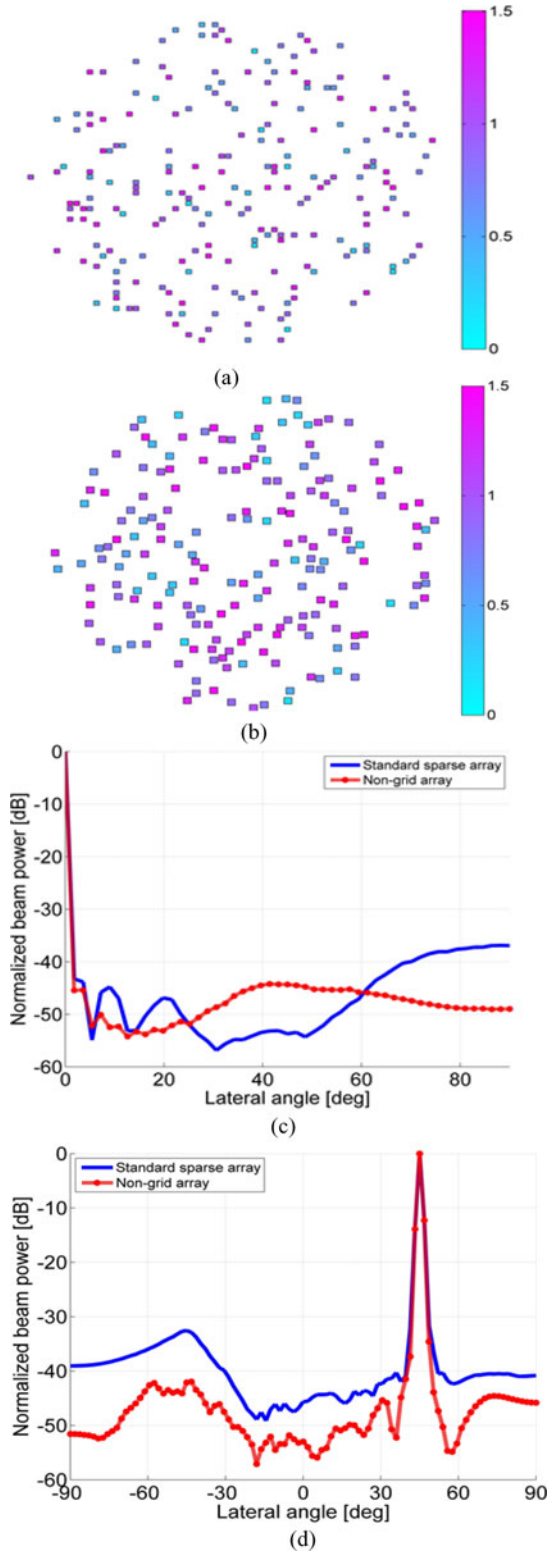

Fig. 8. Optimized 64 × 64 sparse arrays: (a) standard sparse array with 216 square elements sized at λ/2; (b) nongrid sparse array with 186 square elements sized at 4λ/5 (the color bars represent the elements' apodization); (c) unsteered beam profiles along the lateral direction; (d) steered beam profiles for a 45° lateral angle and 45° elevation angle. (In (c), the angles are restricted to the interval [0°, 90°] because of symmetry and in (c) and (d) only the beam profiles in the lateral direction are presented because they are identical to those in the elevation direction.)

TABLE II
CHARACTERISTICS OF THE 64 × 64 AND 64 × 16 DENSE ARRAYS AND OF THE CORRESPONDING OPTIMIZED SPARSE ARRAYS

		Dense array		Standard sparse array		Non-grid sparse array	
		64x64	64x16	64x64	64x16	64x64	64x16
Number of elements		4096	1024	216	177	186	101
Element size		λ/2	λ/2	λ/2	λ/2	4λ/5	4λ/5
Lateral / Elevation main lobe width at −6 dB (degree)		0.7	0.7 / 6.2	0.6	0.6 / 4.8	0.6	0.6 / 3.9
Lateral/ Elevation grating-lobe (dB)	On-axis	−36.3	−35.6 / −16.2	−37.1	−39.8 / −18.4	−42	−41.8 / −40.6
	Off-axis (Steering)	−29	−29.1 / −18.6	−32.5	−34.9 / −24.5	−41	−39.4 / −33.1
Active surface (mm²)		198.2	49.5	10.4	8.6	23	12.5

constraint ($p_s = -40$ dB), but the grating-lobe level of the non-grid sparse array is 6 dB lower.

To evaluate the performance of the optimized arrays in the case of steering, the scatterer was placed at a 40-mm depth and at 45° in both the lateral and elevation directions. The results displayed in Fig. 8(d) show that while both arrays satisfy the side-lobe constraint (max: 40 dB), the grating lobe level of the standard sparse array is 10 dB higher (−32 dB versus −42 dB). In short, with 14% fewer elements than the standard sparse array, the nongrid sparse array has fewer grating lobes and an increased active surface.

Table II summarizes the performance obtained with the dense, standard sparse, and nongrid sparse arrays, for both the square and rectangular probes.

D. Synthetic Imaging Examples

To further validate the proposed approach, we simulated the imaging of two phantoms—a tissue phantom with a biopsy needle and a cyst phantom—using the 64 × 16 array and the 64 × 64 array in the two cases, respectively.

The first numerical phantom is a 50 mm × 50 mm × 30 mm tissue volume in which a needle is inserted. The homogeneous tissue region is filled with scatterers whose positions are randomly sampled and whose strengths follow a Gaussian distribution. The needle is cylindrical, 20 mm long with a 0.3-mm radius, characterized by a scatterer concentration 50 times higher than that of the tissue. The TX focus is at 60 mm and the foci in reception are located at 35, 45, 55, and 65 mm. The images obtained with the dense, standard sparse, and nongrid sparse arrays described in the previous section are shown in Fig. 9 together with a reference A-line intersecting the needle. All data are normalized to the peak echo value obtained from the needle using the dense array. Compared to the dense array, the energy loss is about −18 dB for both the nongrid and standard sparse arrays. The needle echo is 26 dB higher than tissue for the dense array and 25 dB higher for both the nongrid and standard sparse arrays.

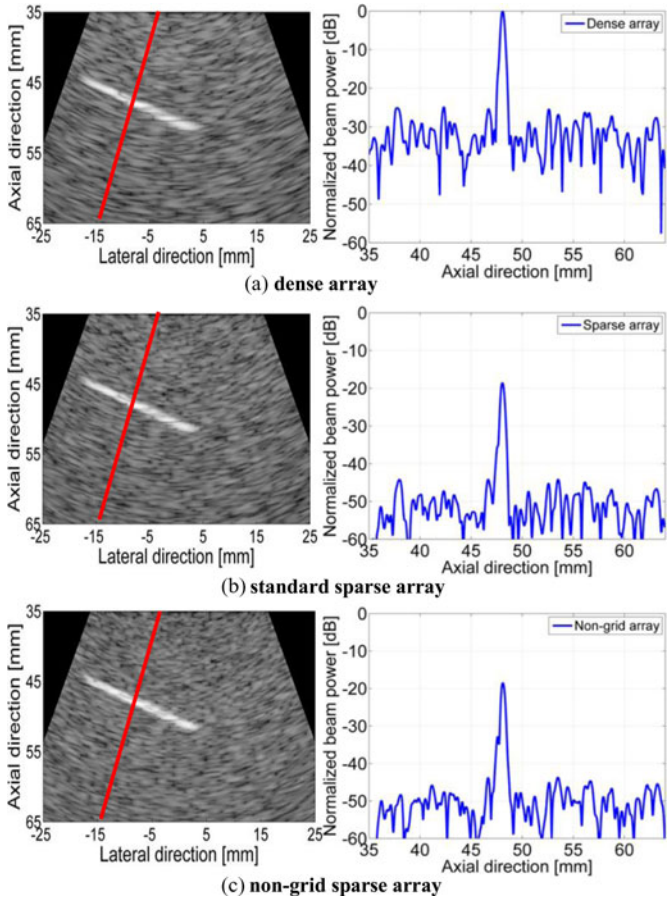

Fig. 9. Imaging of a numerical phantom (needle inserted in a homogeneous tissue volume): frames and A-lines obtained with (a) the 64 × 16 dense array, (b) the optimized standard sparse array with 177 elements, and (c) the optimized nongrid sparse array with 101 elements.

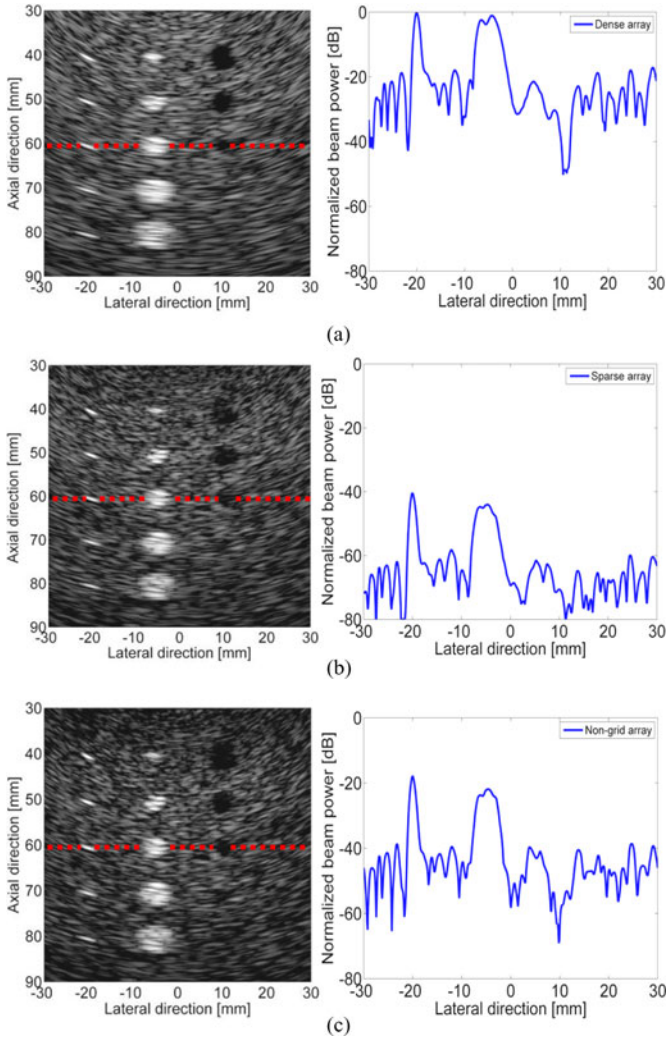

Fig. 10. Imaging of a cyst phantom: frames and 60-mm-depth profiles obtained with (a) the 64 × 64 dense array, (b) the optimized standard sparse array with 256 elements, and (c) the optimized nongrid sparse array with 256 elements.

The second numerical phantom is a cyst phantom 60 mm × 10 mm × 60 mm. There are five anechoic cysts (zero amplitude) aligned at different depths and parallel to five hyperechoic cysts (amplitude ten times higher than the tissue amplitude). The cysts have a spherical shape with their diameter ranging from 2 to 6 mm. Five hyperechoic point scatterers are also placed at −20 mm in the lateral direction. In this case, the simulations were performed using the same number of active elements (256) for both the standard and nongrid 64 × 64 sparse arrays. The TX focus is at 60 mm and the foci in reception are located at 30, 50, 70, and 90 mm. Fig. 10 displays the simulation results for (a) the dense array, (b) the standard sparse array, and (c) the nongrid array. The B-mode images are shown together with the beam profiles at a 60-mm depth. All the data are normalized to the peak echo value in the profile obtained using the dense array.

In the nongrid array, compared to the dense array, the energy loss is about −18 dB whereas it is about −40 dB in the standard sparse array. The difference between the background and the hyperechoic cyst (at a 60-mm depth) is 18 dB for both the dense and the standard sparse arrays, and 21 dB for the nongrid sparse array. This contrast improvement can be explained by the lower grating-lobe level of the nongrid sparse array.

VI. Discussion and Conclusion

Compared to approaches using dense arrays and microbeamforming in the probe handle, the proposed nongrid method is slightly less effective but much less expensive; it does not need special electronics to make the number of system channels compatible with a large number of elements. Furthermore, the proposed random-element positioning approach has the following advantages over standard sparse arrays. First, the irregular positioning of the elements significantly reduces the grating lobes, thus making wider sector scans possible. Second, it allows working with fewer elements while achieving better performance. Third, elements wider than half the wavelength can be used, which provides a better SNR ratio (better sensitivity) by increasing the active surface of the probe [31], [33]. An appropriate choice of the active elements and their weighting coefficients reduce the side lobes and maintain the main-lobe width of sparse arrays. To this end, we have proposed a new cost function that significantly reduces the complexity of the problem and a new SA algorithm that satisfies the global convergence assumptions of finite-time annealing that is quite easy to implement.

Our experiments demonstrate the practical benefits of the method. In the rectangular probe, compared to the optimal standard sparse array, the optimized nongrid sparse array has 43% fewer elements, a thinner main lobe in the elevation direction, significantly lower grating-lobe levels (2-dB and 22-dB reduction in the lateral and elevation directions, respectively). For the square array, the nongrid approach provides an element number reduction of 14%, a grating lobe reduction of 10 dB and a sidelobe reduction of 5 dB compared to the standard sparse approach (see Fig. 8). The beam can be steered from -45° to 45° without excessive deterioration of the beam profile, contrary to the majority of the optimization-based techniques proposed in the literature. In addition, our biopsy needle and cyst phantom imaging simulations show that the proposed approach improves the resolution without increasing the SNR ratio. The results confirm that the proposed technique can actually work with large 2-D arrays like those currently commercially available (e.g., 3000 elements in cardiac arrays [3]).

Nongrid sparse arrays can be made with capacitive micromachined ultrasonic transducers (CMUTs) [34]. They are even feasible using piezoelectric probes, although with some limitations (a minimum interelement distance must be kept) [35]. Progress in manufacturing technology will provide the required flexibility for random-element positioning.

Our future directions will be 1) to further improve the sparse-array design by letting the element positions be part of the optimization process and 2) to conduct experiments using the ULA-OP research platform [36], [37] with small array probes.

REFERENCES

[1] A. Fenster, D. B. Downey, and H. N. Cardinal, "Three-dimensional ultrasound imaging," *Phys. Med. Biol.*, vol. 46, pp. 67–99, 2001.

[2] J. D. Larson, "2-D phased array ultrasound imaging system with distributed phasing," U.S. Patent 522 993 320, Jul. 1993.

[3] B. Savord and R. Solomon, "Fully sampled matrix transducer for real time 3D ultrasonic imaging," in *Proc. IEEE Ultrason. Symp.*, 2003, vol. 1, pp. 945–953.

[4] M. I. Fuller, E. V. Brush, M. D. C. Eames, T. N. Blalock, J. A. Hossack, and W. F. Walker, "The sonic window: second generation prototype of low-cost, fully-integrated, pocket-sized medical ultrasound device," in *Proc. IEEE Ultrason. Symp.*, 2005, vol. 1, pp. 273–276.

[5] W. Lee, S. F. Idriss, P. D. Wolf, and S. W. Smith, "A miniaturized catheter 2-D array for real-time, 3-D intracardiac echocardiography," *IEEE Trans. Ultrason., Ferroelectr. Freq. Control*, vol. 51, no. 10, pp. 1334–1346, Oct. 2004.

[6] A. Austeng and S. Holm, "Sparse 2-D arrays for 3-D phased array imaging—design methods," *IEEE Trans. Ultrason., Ferroelectr. Freq. Control*, vol. 49, no. 8, pp. 1073–1086, Aug. 2002.

[7] A. Trucco, "Thinning and weighting of large planar arrays by simulated annealing," *IEEE Trans. Ultrason., Ferroelectr. Freq. Control*, vol. 46, no. 2,, pp. 347–355, Mar. 1999.

[8] P. Chen, B. Shen, L. Zhou, and Y. Chen, "Optimized simulated annealing algorithm for thinning and weighting large planar arrays," *J. Zhejiang Univ.— Sci. C*, vol. 11, pp. 261–269, 2010.

[9] M. Uherčík, J. Kybic, H. Liebgott, and C. Cachard, "Model fitting using RANSAC for surgical tool localization in 3-D ultrasound images," *IEEE Trans. Biomed. Eng.*, vol. 57, no. 8, pp. 1907–1916, Aug. 2010.

[10] N. M. Daher and J. T. Yen, "2-D array for 3-D ultrasound imaging using synthetic aperture techniques," *IEEE Trans. Ultrason., Ferroelectr. Freq. Control*, vol. 53, no. 5, pp. 912–924, May 2006.

[11] A. T. Fernandez, K. L. Gammelmark, J. J. Dahl, C. G. Keen, R. C. Gauss, and G. E. Trahey, "Synthetic elevation beamforming and image acquisition capabilities using an 8×128 1.75D array," *IEEE Trans. Ultrason., Ferroelectr. Freq. Control*, vol. 50, no. 1, pp. 40–57, Jan. 2003.

[12] S. S. Brunke and G. R. Lockwood, "Broad-bandwidth radiation patterns of sparse two-dimensional vernier arrays," *IEEE Trans. Ultrason., Ferroelectr. Freq. Control*, vol. 44, no. 5, pp. 1101–1109, Sep. 1997.

[13] C. E. Morton and G. R. Lockwood, "Theoretical assessment of a crossed electrode 2-D array for 3-D imaging," in *Proc. IEEE Ultrason. Symp.*, Honolulu, HI, USA, 2003, vol. 1, pp. 968–971.

[14] J. T. Yen and S. W. Smith, "Real-time rectilinear volumetric imaging using a periodic array," *Ultrasound Med. Biol.*, vol. 28, pp. 923–931, 2002.

[15] C. H. Seo and J. T. Yen, "A 256×256 2-D array transducer with row-column addressing for 3-D rectilinear imaging," *IEEE Trans. Ultrason., Ferroelectr. Freq. Control*, vol. 56, no. 4, pp. 837–847, Apr. 2009.

[16] D. H. Turnbull and F. S. Foster, "Beam steering with pulsed two-dimensional transducer arrays," *IEEE Trans. Ultrason., Ferroelectr. Freq. Control*, vol. 38, no. 4, pp. 320–333, Jul. 1991.

[17] B. Diarra, H. Liebgott, P. Tortoli, and C. Cachard, "2D matrix array optimization by simulated annealing for 3D hepatic imaging," in *Proc. IEEE Ultrason. Symp.*, 2011, pp. 1595–1598.

[18] P. K. Weber, R. M. Schmitt, B. D. Tylkowski, and J. Steck, "Optimization of random sparse 2-D transducer arrays for 3-D electronic beam steering and focusing," in *Proc. IEEE Ultrason. Symp.*, 1994, vol. 3, pp. 1503–1506.

[19] B. Hajek, "Cooling schedules for optimal annealing," *Math. Oper. Res.*, vol. 13, pp. 311–329, 1988.

[20] O. Catoni, "Rough large deviation estimates for simulated annealing: Application to exponential schedules," *Annu. Probab.*, vol. 20, pp. 1109–1146, 1992.

[21] M. C. Robini and P.-J. Reissman, "From simulated annealing to stochastic continuation: a new trend in combinatorial optimization," *J. Global Optimization*, vol. 56, no. 1, pp. 185–215, 2013.

[22] M. C. Robini, "Theoretically grounded acceleration techniques for simulated annealing," in *Handbook of Optimization, From Classical to Modern Approach,* (volume 38 of Intelligent Systems Reference Series, Intell. Syst. Ref. Libr.), I. Zelinka, V. Snasel, and A. Abraham, Eds. New York, NY, USA: Springer, 2012, pp. 311–336.

[23] A. Trucco, M. Palmese, and S. Repetto, "Devising an affordable sonar system for underwater 3-D vision," *IEEE Trans. Instrum. Meas.*, vol. 57, no. 10, pp. 2348–2354, Oct. 2008.

[24] R. O. Nielsen, *Sonar Signal Processing*. Norwood, MA, USA: Artech House, 1991.

[25] E. J. Candès, M. B. Wakin, and S. P. Boyd, "Enhancing sparsity by reweighted ℓ 1 minimization," *J. Fourier Anal. Appl.*, vol. 14, pp. 877–905, 2008.

[26] I. Daubechies, R. DeVore, M. Fornasier, and C. S. Güntürk, "Iteratively reweighted least squares minimization for sparse recovery," *Commun. Pure Appl. Math.*, vol. 63, pp. 1–38, 2010.

[27] P. J. Van Laarhoven and E. H. Aarts, *Simulated Annealing: Theory and Applications*. New York, NY, USA: Springer, 1987.

[28] M. C. Robini, T. Rastello, and I. E. Magnin, "Simulated annealing, acceleration techniques, and image restoration," *IEEE Trans. Image Process.*, vol. 8, no. 10, pp. 1374–1387, Oct. 1999.

[29] J. A. Jensen, "FIELD: A program for simulating ultrasound systems," in *Proc. 10th Nordic-Baltic Conf. Biomed. Imag.*, vol. 34, 1996, pp. 351–353.

[30] J. A. Jensen and N. B. Svendsen, "Calculation of pressure fields from arbitrarily shaped, apodized, and excited ultrasound transducers," *IEEE Trans. Ultrason., Ferroelectr. Freq. Control*, vol. 39, no. 2, pp. 262–267, Mar. 1992.

[31] T. Kojima, "Matrix array transducer and flexible matrix arry transducer," in *Proc. IEEE Ultrason. Symp.*, 1986, pp. 649–654.

[32] A. Trucco, "Synthesizing wide-band sparse arrays by simulated annealing," in *Proc. MTS/IEEE Conf. Exhib. OCEANS*, 2001, pp. 989–994.

[33] J.-Y. Lu and J. F. Greenleaf, "A study of two-dimensional array transducers for limited diffraction beams," *IEEE Trans. Ultrason., Ferroelectr. Freq. Control*, vol. 41, no. 5, pp. 724–739, Sep. 1994.

[34] M. I. Haller and B. T. Khuri-Yakub, "A surface micromachined electrostatic ultrasonic air transducer," in *Proc. IEEE Ultrason. Symp.*, 1994, vol. 2, pp. 1241–1244.

[35] G. Fleury, Personal communication, Imasonic, Besançon, France, 2013.

[36] P. Tortoli, L. Bassi, E. Boni, A. Dallai, F. Guidi, and S. Ricci, "ULA-OP: An advanced open platform for ultrasound research," *IEEE Trans. Ultrason., Ferroelectr. Freq. Control*, vol. 56, pp. 2207–2216, 2009.

[37] E. Boni, L. Bassi, A. Dallai, F. Guidi, A. Ramalli, S. Ricci, J. Housden, and P. Tortoli, "A reconfigurable and programmable FPGA-based system for nonstandard ultrasound methods," *IEEE Trans. Ultrason., Ferroelectr. Freq. Control*, vol. 59, no. 7, pp. 1378–1385, 2012.

Authors' photographs and biographies not available at the time of publication.